Albetran, H.M.M. and Haroosh, H.J.M. and Dong, Y. and Prida, V. and O'Connor, B. and Low, I.M. 2014. Applied Physics A: Materials Science and Processing. 116 (1): pp. 161-169.

Phase Transformations and Crystallization Kinetics in Electrospun TiO_2 Nanofibers in Air and Argon Atmospheres

H. Albetran[a,b], **H. Haroosh**[c], **Y. Dong**[d], **V.M. Prida**[e], **B. H. O'Connor**[a] and **I. M. Low**[a*]

[a] Department of Imaging and Applied Physics, Curtin University, Perth, WA 6845, Australia

[b] Department of Physics, College of Education, University of Dammam, Dammam 31451, Saudi Arabia.

[c] Department of Chemical Engineering, Curtin University, Perth, WA 6845, Australia.

[d] Department of Mechanical Engineering, Curtin University, Perth, WA 6845, Australia.

[e] Department of Physics, University of Oviedo, Calvo Sotelo s/n, 33007-Oviedo, Spain.

*Corresponding author. Tel.: +618 9266 7544; fax: +61 8 92662377.

E-mail address: j.low@curtin.edu.au

Abstract: The effects of atmospheric air and argon environments on thermal-induced phase transformations in electrospun TiO_2 nanofibers have been investigated *in-situ* using synchrotron radiation diffraction. Diffraction results showed that the as-synthesized TiO_2 nanofibers were initially amorphous, but crystallized to form anatase and rutile after thermal annealing in air or argon at elevated temperatures. The crystallization temperature of anatase was delayed by 100 ^oC in argon relative to in air, and the transformation of anatase into rutile occurs faster in argon atmosphere than in air due to the formation of oxygen vacancies. Non-linear strains formed in both polymorphs and the substantial elevation of rutile thermal expansion pointed to strain anisotropy in the rutile phase and the concomitant fibre-breakage.

***Keywords*:** Synchrotron radiation diffraction, anatase, rutile, electrospun nanofibers, thermal expansion.

1 Introduction

Titanium dioxide (TiO_2) is one of the most widely studied materials due to its high photo-activity, photo-durability, mechanical robustness, low cost, and chemical and biological inertness [1-6]. Titanium dioxide has three polymorphs: anatase, brookite, and rutile [7-10]. Anatase and rutile are the two main polymorphs that exhibit different properties and thus different photocatalytic performances. They both have tetragonal crystal structures, but different space groups and atoms per unit cell (Z), space group *I4/amd* and Z = 4 for anatase and $P4_2/mnm$ and Z = 2 for rutile [9, 11]. At room temperature, the lattice parameters of anatase are $a = b = 0.3785$ nm and $c = 0.9514$ nm, while for rutile are $a = b = 0.4594$ nm and $c = 0.29589$ nm [12]. These differences in the inter-atomic spacing and crystal structures for anatase and rutile can result in a different densities and electronic band structures. Anatase is considered more photochemically active than rutile by virtue of its lower rates of electronic recombination and higher surface absorptive capacity [13]. However, recent work has indicated that a mixed-phase TiO_2 tends to make a superior photocatalyst than a single-phase TiO_2. For example, a mixed-phase sample of 70% anatase and 30% rutile has been found as the best photocatalyst for wastewater treatment [14]. Similarly, commercial TiO_2 photocatalyst (P-25) that contains 80 wt% anatase and 20 wt% rutile has been observed to exhibit excellent photocatalytic reactions [12].

The optimum composition in terms of the anatase and rutile levels for maximum photocatalytic performance can be achieved by thermal annealing. In general, anatase forms from amorphous TiO_2 at low temperatures which subsequently transforms to rutile at higher temperatures [15, 16]. The transformation is affected by various conditions which include the synthesis method, the amount of impurities, temperature, calcination time and atmosphere type [15, 17]. Reaction atmospheres have been observed to have a significant influence on the thermal transformation of TiO_2 phases because oxygen defect levels and interstitial titanium ion levels are influenced by the type of atmosphere [15, 18]. The effects of air, vacuum, argon, argon–chlorine mixture, hydrogen, steam and nitrogen on the anatase to rutile phase transformation have been reported [18]. For TiO_2 films, the amorphous to anatase and anatase to rutile phase transformations were observed to occur at a lower

temperature when annealed in a hydrogen atmosphere than in air or vacuum [19]. The rate of anatase to rutile phase transformation was found to decrease in vacuum but increase in hydrogen atmosphere due to the formation of either titanium interstitials or oxygen vacancies. Since the phase transition involves an overall shrinkage of the oxygen structure and a cooperative movement of ions, the formation of oxygen vacancies would accelerate the phase transition and vice versa for the formation of titanium interstitials [15].

Nanostructured TiO_2 with elongated morphology exhibits high surface area to volume ratio which is of great significance for increasing the decomposition rate of organic pollutants because photocatalytic reactions take place rapidly and drastically on the surface of the catalyst [14, 20]. Hitherto, various techniques have been used to synthesise nanostructured TiO_2 with various morphologies (e.g. nanowires, nanorods, nanotubes, and nanofibers). These include microemulsion, sol–gel, hydrothermal and vapor deposition [8, 21]. Elongated nanostructures are of particular importance, as long and thin nanotubes or nanofibers can provide a high specific surface area for photocatalysis [9]. Furthermore, a variety of techniques, such as self-assembly, evaporation, anodisation, and electro-spinning, have been developed for fabricating one-dimensional nano- TiO_2 [1, 22, 23]. Among the fabrication methods, electro-spinning is a simple and cost-effective technique applicable at industrial levels for fabricating one-dimensional nanofibers [22-25]. In this process, a solution of polymer and TiO_2 precursor is ejected through a needle in a high electric field whereby composite nanofibers of polymer and amorphous TiO_2 are formed [25-29]. To the best of our knowledge, the effect of atmospheres on the *in-situ* crystallization of anatase and rutile in electrospun TiO_2 nanofibers has not been previously reported.

In the present work, the effect of air and argon atmosphere on the transformation of anatase into rutile and the *in-situ* crystallization kinetics of TiO_2 nanofibers were investigated using synchrotron radiation diffraction (SRD) over the temperature range of 25–900 °C. TiO_2 nanofibers were synthesized using electro–spinning and their morphology, structure and thermal expansion were characterized by scanning electron microscopy (SEM) and associated energy dispersive spectroscopy (EDS), and high-temperature synchrotron radiation diffraction (SRD).

2 Experimental procedure

2.1 Material synthesis

A homogenous sol–gel precursor solution was prepared by mixing titanium isopropoxide (TIP) (M_w = 284.22 g/mol, 97% purity – sourced from Sigma-Aldrich), acetic acid (M_w = 60.05 g/mol, 99.7% purity – Sigma-Aldrich), and ethanol (M_w = 46.07 g/mol, 99.5% purity – Sigma-Aldrich) in a fixed volume ratio of 3:1:3, respectively. The sol–gel was stirred in a capped bottle for 5 min, and then, 12 wt% of poly-vinyl pyrrolidone (PVP) (M_w = 1300000 g/mol, 100% purity – Sigma-Aldrich) was dissolved in the solution at 40 °C for 1 h using a stirrer. In order to achieve complete dissolution and mixing, the sol–gel solution precursor was stirred ultrasonically for 5 min before it was loaded into a 10 ml plastic syringe with a 25–gauge stainless steel needle. An electro-spinning unit (Gamma High Voltage Research, USA) with a high voltage power supply was used to provide 25 kV between the needle and a mesh collector covered by an aluminium foil at a distance of approximately 12 cm. A syringe pump (Chemyx Inc. USA) was used to control the solution flow rate at 2 ml/h during the process of electrospinning.

2.2 In situ high-temperature synchrotron radiation diffraction (SRD)

The *in-situ* crystallization behavior of electrospun TiO_2 nanofibers was evaluated using high-temperature SRD in air and in argon. The SRD measurements were conducted at the Powder Diffraction Beamline at the Australian Synchrotron. The specimens were mounted on an Anton Parr HTK 16 hot platinum stage and heated with an Anton Paar HTK20 furnace. The SRD data were collected at an incident angle of 3^o and wavelength of 0.1126 nm.

The SRD patterns were acquired initially at ambient temperature and then in steps of 100 °C from 200 °C to 900 °C at a rate of 10 °C/min with a data acquisition time of 10 min per pattern. Each pattern was measured over the angular range 2θ = 5°–84°. The SRD data were analysed using Rietveld pattern-fitting with the Rietica program (version 2.1) [30], to compute the relative crystalline phase abundances, and the lattice parameters of anatase and rutile at each temperature [31]. The parameters optimized in the Rietveld refinements were the pattern background, 2θ-zero, and for each phase the scale factor, lattice parameters and the peak shape

parameters. The Rietveld refinements were conducted with the crystal structures of anatase (ICSD 202242) and rutile (ICSD 64987). The Jade (version 6) program was used to perform peak broadening analyses in order to obtain the crystalline size (L) and the strain (ε) for each two phase as a function of temperature, using Williamson-Hall (W-H) plots [32]:

$$\beta \cos\theta = \lambda / L + 4\varepsilon \sin\theta \qquad (1)$$

where λ is the x-ray wavelength, θ is the Bragg angle, and β is the integral breath of a peak. The crystallite size (L) was estimated from the y-intercept, and the strain (ε) from the slope of a linear fit to the data.

2.3 Scanning electron microscopy

The morphologies of the electrospun TiO_2 nanofibers were examined using an EVO 40XVP scanning electron microscope with an accelerating voltage of 15 kV. Prior to the microstructure observations, the samples were coated with platinum to avoid charging. The SEM images of as–spun nanofibers were taken using secondary and backscattered electrons at working distances of 4 mm and 4.5 mm, respectively. The samples were characterized again at the same accelerating voltage after thermal annealing in air and argon atmospheres. Associated energy dispersive X-ray spectroscopy (EDS) with an acceleration voltage of 10 kV, magnification of 606, silicon detector and zero electronic beam tilt was used to analyse the elemental compositions of the SEM-imaged materials.

3 Results and discussion

3.1 Microstructures of electrospun TiO_2 nanofibers

Fig. 1 illustrates the SEM images of electrospun nanofibers using secondary and backscattered electrons, before and after thermal annealing. In the former, the nanofibers have smooth surfaces with a random distribution and annealing. The average diameter of electrospun nanofibers was 614 ± 190 nm, with the fibers being well-dispersed within the PVP matrix, as shown in Fig. 1 (a) and (b).

However, after thermal annealing at 900 °C, the average diameters of the nanofibers shrank by approximately 42% in air (Fig. 1(c)) and 47% in argon (Fig. 1(d)) compared to as-spun nanofibers, due to the loss of the organic binder during heating. The average diameters of nanofibers were 358 ± 195 nm in air and 328 ± 113 nm in argon. In argon, the nanofibers were partially broken while in air the extent of fiber breakage was less. A probable reason for the fiber breakage could be due to damage arising from sample handling or during the SEM examination. A more likely explanation is the thermal expansion anisotropy of rutile and the associated strains induced at elevated temperatures (see Table 2, and the thermal expansion section).

The EDS spectrum of as-spun TiO_2/PVP nanofibers in Fig. 2 (b) showed strong signatures for Ti, O and C, with the C content being due to the PVP polymer binder. The EDS spectrum of the nanofiber sample after thermal annealing at 900 °C (Fig. 2 (d)) was similar to that for the original material, other than showing the absence of the C peak due to the complete loss of the organic matrix. The same observation was made when the nanofibers were heated in argon.

3.2 Effect of environmental atmosphere on the phase transitions during thermal annealing

Fig. 3 shows the effect of atmosphere on the *in-situ* crystallization kinetics of as-synthesized TiO_2 nanofibers over the temperature range 25–900 °C, as revealed by SRD. The SRD patterns showed Pt peaks due to the Pt sample mount which were ignored in the calculations. The TiO_2/PVP nanofibers were initially amorphous as shown by the pronounced amorphous hump for the 25 °C pattern and the absence of diffraction peaks. By 200 °C the amorphous feature had largely disappeared and had gone completely by 400 °C. In air (Fig. 3 (a)), anatase and rutile were first observed at 600 °C and 700 °C, respectively. However, in argon, both anatase and rutile were first observed at 700 °C (Fig. 3 (b)), so that the initial crystallization of anatase was delayed by 100 °C in argon compared with air. The reason for this delay in the formation of anatase in argon atmosphere may be attributed to the lack of oxygen. It appears that atmospheric oxygen accelerates the transformation from amorphous TiO_2 into anatase. Moreover, the partial pressure of oxygen also influences the rate of anatase-to-rutile transformation, becoming faster in argon atmosphere which has

a much lower oxygen partial pressure [15]. Defects of oxygen vacancies created in argon atmosphere by the low partial pressure of oxygen accelerates the anatase-to-rutile transformation, which involves the breaking of anatase Ti-O bonds and reforming of rutile Ti-O bonds [12, 18]. Hence, the transformation rate from anatase into rutile was faster in argon than in air atmosphere by virtue of oxygen vacancies (see Table 1).

The fraction of anatase-to-rutile transformation can be estimated using the Spurr equation [33]:

$$x = 1/[1 + 0.8(I_A / I_R)] \qquad (2)$$

where I_A and I_R are the X-ray integrated intensities of anatase (101) reflection and rutile (110) reflection, respectively. Table 1 shows the fraction of anatase-to-rutile transformation as a function of temperature in air and in argon as determined using the Spurr equation and Rietveld method. It is evident that the weight fraction of rutile increased dramatically as the temperature increased by virtue of the transformation of metastable anatase into rutile at elevated temperatures. The rate of anatase-to-rutile transformation was also observed to increase faster in argon than in air. This enhanced transformation rate may be attributed to the formation of oxygen vacancies in TiO_2 annealed in argon [12]. The formation of oxygen vacancies would accelerate the phase transition since it involves an overall shrinkage of the oxygen structure and a cooperative movement of ions [15].

Fig. 4 shows the intensities of anatase (101) and rutile (110) peaks over the temperature range 600–900 °C. Because the most intense peaks for both crystalline phases have virtually the same Reference Intensity Ratio, the intensity-temperature plots should be seen as 'relative concentration-temperature' plots, with the sum of the anatase and rutile peaks being proportional to the total concentration of crystalline TiO_2. The formation of crystalline TiO_2 was first observed at 600 °C and increased steadily up to 900 °C, when heating in both air and argon. It is evident that the amorphous TiO_2 was not completely converted to crystalline TiO_2 by 900 °C. Fig. 4 also shows the progressive growth of rutile after the formation, whereas the anatase concentration steadily reduces beyond approximately 800 °C due to

transformation to rutile. Overall, Fig. 4 is consistent with the transformation of anatase into rutile becoming more likely with increases in temperature. This discussion is extended below when the results on relative amounts of anatase and rutile with temperature in Fig. 6 are considered.

Fig. 5 shows the typical SRD plots from Rietveld analysis for data measured in air and argon at 800 °C. In general, the quality or goodness of fit is gauged by the values of weighted pattern R-factor (R_{wp}), the expected R-factor (R_{exp}), and the derived Bragg R-factor (R_B) [30]. In this work, values obtained for air and argon atmospheres were R_{wp} = 13.0 and 10.0, R_{exp} = 3.7 and 4.6, R_B (anatase) = 4.6 and 4.9, and R_B (rutile) = 7.3 and 4.2, respectively.

Fig. 6 shows the variation with temperature of the relative amounts of anatase and rutile from Rietveld analysis, which supplements the information shown in Fig. 4. The conversion of crystalline anatase to rutile in both air and argon atmospheres are clearly indicated. The results show that the conversion is less rapid in air than in argon. At 600 °C, anatase formed in air but not yet in argon. In argon at 700 °C, anatase comprised 85% of the crystalline TiO_2, and 95% of the total in air. By 800 °C the abundance of anatase in crystalline TiO_2 falls to 76% in air and 50% in argon, and then by 900 °C to 35% in air and to 14% in argon. In addition, the phase content of rutile increased dramatically as the temperature increased by virtue of the transformation of metastable anatase into rutile. Rutile formed at 700 °C in both atmospheres but with different abundances. It increased from about 15% at 700 °C to well over 85% at 900 °C in argon atmosphere. However, in air, it increased from 5% up to only 65% for the same temperature range.

Fig. 7 shows the effect of temperature on the growth of anatase and rutile crystallites according to atmosphere. The average crystallite size for anatase was ~13 nm at 700 °C in air and increased linearly for both atmospheres, to ~30 nm at 900 °C. The significantly larger rutile crystallite sizes were ~18 nm at 700 °C in both air and argon, but grew to ~37 nm in air and ~40 nm in argon at 900 °C. Therefore, the atmosphere had an insignificant effect on crystallite growth. The crystallite growth with temperature behaviour is attributed to the conversion of amorphous material to crystalline TiO_2 through an atomic diffusion-controlled nucleation and growth process. The gradients of the linear regressions for the plots in Fig. 5 amount to approximately 1.5–2% volumetric growth per degree increase in

temperature. This diffusion growth is orders of magnitude higher than that due to lattice thermal expansion (see Fig. 9).

The effect of temperature on the average lattice strain of both anatase and rutile for both atmospheres is shown in Fig. 8. It can be seen that the initial strain present in both phases is progressively relieved as the temperature increases. The observed strain relief is consistent with crystallite-crystalline interactions being negligible up to the maximum temperature considered in the study, at which point there is still substantial amorphous TiO_2 present. The higher strains observed for the anatase phase in air is consistent with the the finding of Nicula et al. [34] who reported that the anatase phase exhibits larger strain values than rutile in titania powders over 400–850 °C.

The variations of unit-cell parameters and cell-volumes for anatase and rutile with temperature are shown in Fig. 9 (a) and (b), and Fig. 10, and the corresponding linear and volumetric thermal expansion coefficients (TECs) are provided in Table 2. The unit-cell parameters and cell-volume**,** for both phases in air and argon atmospheres increased linearly with temperature, as expected. The SRD thermal expansion data of Hummer et al. [31] measured with titania powders over the temperature range 25–300 °C, which are included in Table 2, were extrapolated to the temperatures considered in this study. It is seen that the TECs for the anatase in both air and argon compare closely with values reported for crystalline TiO_2 powder. By contrast, the rutile expansion coefficients are higher in argon, and higher again in air. There is also clear evidence for thermal expansion anisotropy in the rutile phase which points to the development of a more pronounced strain in rutile compared with anatase, and with the effect being more pronounced in argon which may explain the rougher appearance and more breakage of the nanofibers at high temperatures compared with heating in air. In addition, for both anatase and rutile, the thermal expansion coefficients (TECs) were higher in air than in argon atmospheres due to the formation of oxygen vacancies in argon atmosphere. However, the linear expansion coefficient ratio of α_a to α_c was ~9% higher in argon than in air, which could be the main reason for the embrittlement of nanofibers. Furthermore, it should be noted that literature equations of anatase and rutile parameters have hitherto been determined at relatively low temperatures, from room

temperature to just over 300 °C using anatase and rutile TiO_2 powders, while the present study examined TiO_2 nanofibers at higher temperatures.

4 Conclusions

The effect of air and argon on the dynamic crystallization behaviour of electrospun TiO_2 nanofibers was investigated *in-situ* using SRD data measured in the temperature range 25–900 °C. The electrospun TiO_2 nanofibers were initially amorphous but crystallized progressively into anatase and rutile at elevated temperatures. In air, anatase was first observed at 600 °C and rutile at 700 °C, but in argon both appeared at 700 °C. The level of crystalline TiO_2 (anatase and rutile) increased monotonically with increase in temperature, with some amorphous TiO_2 still being observed at 900 °C. The rates of anatase to rutile transformation were faster in argon than in air by virtue of oxygen vacancies in the former. The non-linear strain in both polymorphs reduced with temperature, with the strain of anatase in air being elevated. The substantial elevation of rutile thermal expansion pointed to strain anisotropy in the rutile phase and the concomitant fibre-breakage.

Acknowledgments

The authors gratefully acknowledge the Australian Synchrotron (AS122/PDFI/5075) for work supporting. The authors would like to thank Ms. E. Miller and Dr. N. Chen-Tan for assistance with the SEM work, and Ms. K. Haynes, Mr. A. Viereckl and Mr. J. Xiao Hua for laboratory assistance.

References

1. I.M. Low, H. Albetran, V.M. Prida, V. Vega, P. Manurung, M. Ionescu, J. Mater. Res. **28,** 304 (2013)
2. P. Manurung, Y. Putri, W. Simanjuntak, I. M. Low, Ceram. Int. **39**, 255 (2013)
3. P. Zhang, C. Shao, X. Li, M. Zhang, X. Zhang, Y. Sun, Y. Liu, J. Hazard. Mater. **237**–**238**, 331 (2012).
4. C. Yu, L. Wei, X. Li, J. Chen, Q. Fan, J. Yu, Mater. Sci. Eng. B **178,** 344 (2013)
5. X. Pan, Y. Zhao, S. Liu, C.L. Korzeniewski, S. Wang, Z. Fan, ACS Appl. Mater. Interfaces **4**, 3944 (2012)
6. V. J. Babu, A. S. Nair, Z. Peining, S. Ramakrishna, Mater. Lett. **65**, 3064 (2011)
7. G. Liu, L. Wang, H. G. Yang, H. M. Cheng, G. Q. Lu, J. Mater. Chem. **20**,831 (2010)
8. S. Chuangchote, J. Jitputti, T. Sagawa, S. Yoshikawa, ACS Appl. Mater. Interfaces **1,** 1140 (2009)
9. D.W. Kim, N. Enomoto, Z.E. Nakagawa, K. Kawamura, J. Am. Ceram. Soc. **79**, 1095 (1996)
10. R. Liu, L.S. Qiang, W.D. Yang, H.Y. Liu, Mater. Res. Bull. **48**, 1458 (2013)
11. W. Li, C. Ni, H. Lin, C.P. Huang, S.I. Shah, J. Appl. Phys. **96**, 6663 (2004)
12. D. A. Hanaor, C. C. Sorrell, J. Mater. Sci. **46**, 855 (2011)
13. S. Shang, X. Jiao, D. Chen, ACS Appl. Mater. Interfaces **4**, 860 (2012)
14. H. Li, W. Zhang, W. Pan, J. Am. Ceram. Soc. **94**, 3184 (2011)
15. R.D. Shannon, J.A. Pask, J. Am. Ceram. Soc. **48**, 391 (1965)
16. R.A. Eppler, J. Am. Ceram. Soc. **70**, 64 (1987)
17. Y. Iida, S. Ozaki, J. Am. Ceram. Soc. **44**, 120 (1961)
18. J. A. Gamboa, D. M. Pasquevich, J. Am. Ceram. Soc. **75**, 2934 (1992)
19. J. H. Huang, M. S. Wong, Thin Solid Films **520**, 1379 (2011)
20. J.S. Lee, T.J. Ha, M.H. Hong, H.H. Park, Thin Solid Films **529**, 98 (2013)
21. I.M. Low, B. Curtain, M. Philipps, Q.Z. Liu, M. Ionescu, J. Aust. Ceram. Soc. **48**, 198 (2012)
22. V. Vega, V.M. Prida, M.H. Velez, E. Manova, P. Aranda, E.R. Hitzky, M. Vazquez, Nanoscale Res. Lett. **2**, 355 (2007)
23. S. Chuangchote, J. Jitputti, T. Sagawa, S. Yoshikawa, ACS Appl. Mater. Interfaces **1,** 1140 (2009)

24. Z.M. Huang, Y.Z. Zhang, M. Kotaki, S. Ramakrishna, Compos. Sci. Technol. **63**, 2223 (2003)
25. Q. Li, D. J.G. Satur, H. Kim, H.G. Kim, Mater. Lett. **76,** 169 (2012)
26. W. Luo, X. Hu, Y. Sun, Y. Huang, J. Mater. Chem. **22,** 4910 (2012)
27. C. Wessel, R. Ostermann, R. Dersch, B.M. Smarsly, J. Phys. Chem. **C 115**, 362 (2011)
28. H. Li, W. Zhang, W. Pan, J. Am. Ceram. Soc. **94**, 3184 (2011)
29. P. Zhu., A.S. Nair, P. Shengjie, Y. Shengyuan, S. Ramakrishna, ACS Appl. Mater. Interfaces **4**, 581 (2012)
30. W.K. Pang, I.M. Low, J. Am. Ceram. Soc. **93**, 2871 (2010)
31. D.R. Hummer, P. J. Heaney, Powder Diffraction **22**, 352 (2007)
32. G.K. Williamson, W. H. Hall, Acta Metall. **1**, 22 (1953)
33. R.A. Spurr, H. Myers, Anal. Chem. **29**, 760 (1957)
34. R. Nicula, M. Stir, C. Schick, E. Burkel, Thermo. Acta **403**, 129 (2003)

Tables

Table 1: Effect of atmospheres on the fraction of anatase to rutile transformation as a function of temperature.

Temperature (°C)	Air (x)		Argon (x)	
	Spurr Equation [33]	Rietveld method	Spurr Equation [33]	Rietveld Method
700	1.5	4.98(10)	9.2	15.41(28)
800	19.2	24.02(32)	46.5	50.99(28)
900	63.04	64.95(60)	84.5	85.98(49)

Table 2: Linear (α_a, α_c) and Volumetric (β) Thermal Expansion Coefficients (TECs) Calculated from Fig. 9 and 10 at 800 °C.

	TEC×10^{-5} ($°C^{-1}$)		α_a	α_c	β	α_c/α_a
Atmosphere (This study)	Air	Anatase	0.72	0.86	2.29	1.19
		Rutile	1.94	3.12	6.99	1.61
	Argon	Anatase	0.62	0.79	1.99	1.27
		Rutile	1.16	1.98	4.24	1.70
Hummer et al. [31]	Powdered TiO_2 sample in air	Anatase	0.53	1.04	2.17	1.96
		Rutile	0.87	1.01	2.83	1.16

Figure Captions

1. SEM micrographs of as-spun TiO_2 nanofibers imaged with (a) secondary electrons (b) backscattered electrons; and with secondary electrons after cooling from 900 °C, in (c) air and (d) argon atmospheres.
2. (a) SEM micrograph of as-received electrospun TiO_2 nanofibers, and (b) the corresponding EDS spectrum (#1); and (c) SEM micrograph for electrospun TiO_2 nanofibers after cooling in air from 900 °C, and (d) the corresponding EDS spectrum (#2).
3. *In-situ* SRD plots showing the effect of temperature on the crystallization behaviour of as-synthesized TiO_2 nanofibers when heated in 25–900 °C (a) in air, and (b) in argon. [Legend: anatase (A), rutile (R) and platinum (Pt)].
4. The SRD intensities of the anatase (101) and rutile (110) reflections in the range 600–900 °C for TiO_2 nanofibers heated in air and argon. The vertical axis is proportional to the phase concentration for both anatase and rutile, and the sum of the anatase and rutile intensities is proportional to total crystalline titania.
5. SRD Rietveld difference plots for 800 °C SRD data (a) in air and (b) under argon. Measured patterns are indicated by black crosses and calculated patterns by solid red lines. The green residual plot shows the difference between the calculated and the measured patterns. The peak positions for anatase and rutile are indicated by the top and bottom blue bars, respectively.
6. Relative phase abundances of anatase and rutile for the crystalline TiO_2 component in the temperature range 600–900 °C for TiO_2 nanofibers heated in air and argon atmospheres. The phase levels represent the percentages of crystalline TiO_2 at each temperature.
7. Willamson-Hall plot estimates of the effect of temperature on the average crystallite size of (a) anatase and (b) rutile in TiO_2 nanofibers according to temperature.
8. Williamson-Hall plot estimates of mean strain for anatase and rutile crystallites in the range 600–900 °C for TiO_2 nanofibers heated in air and argon atmospheres.
9. Variation with temperature of the lattice parameters for anatase (a) and rutile (b) in air and argon atmospheres.
10. Variation with temperature of the cell volume for anatase and rutile in air and argon atmospheres.

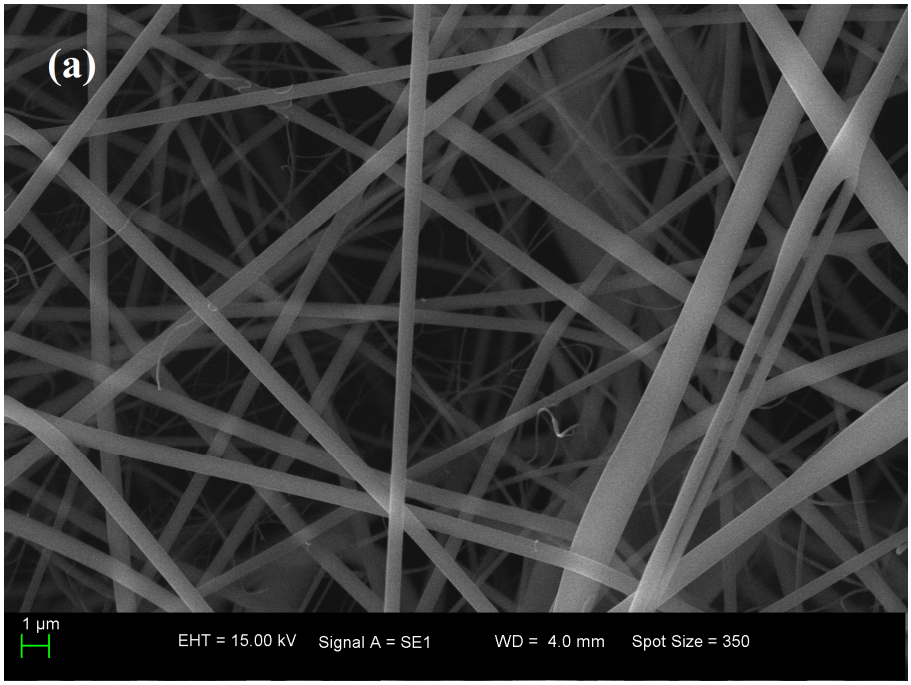
(a)
1 µm
EHT = 15.00 kV
Signal A = SE1
WD = 4.0 mm
Spot Size = 350

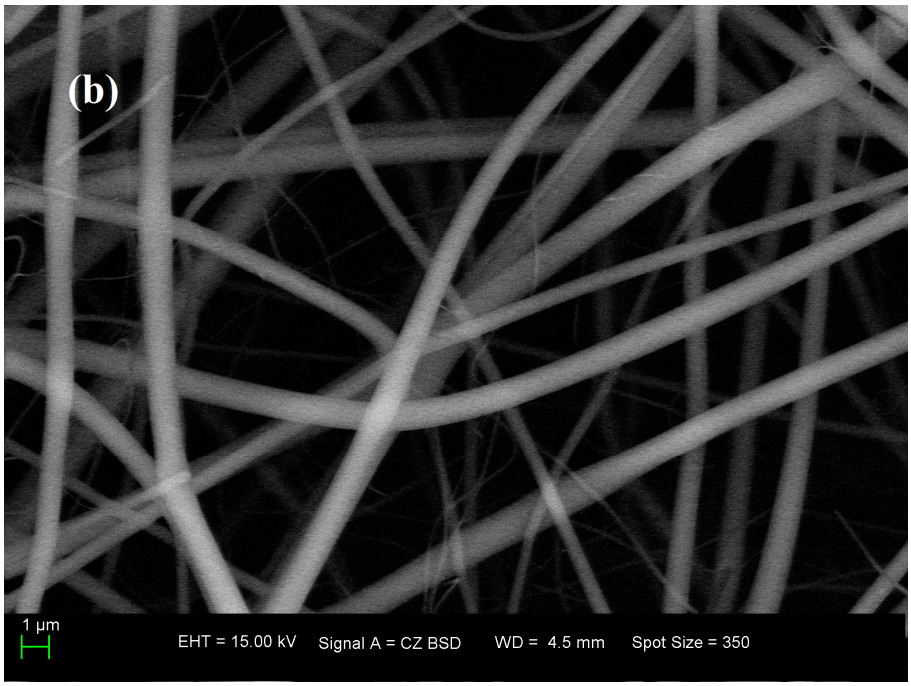
(b)
1 µm
EHT = 15.00 kV
Signal A = CZ BSD
WD = 4.5 mm
Spot Size = 350

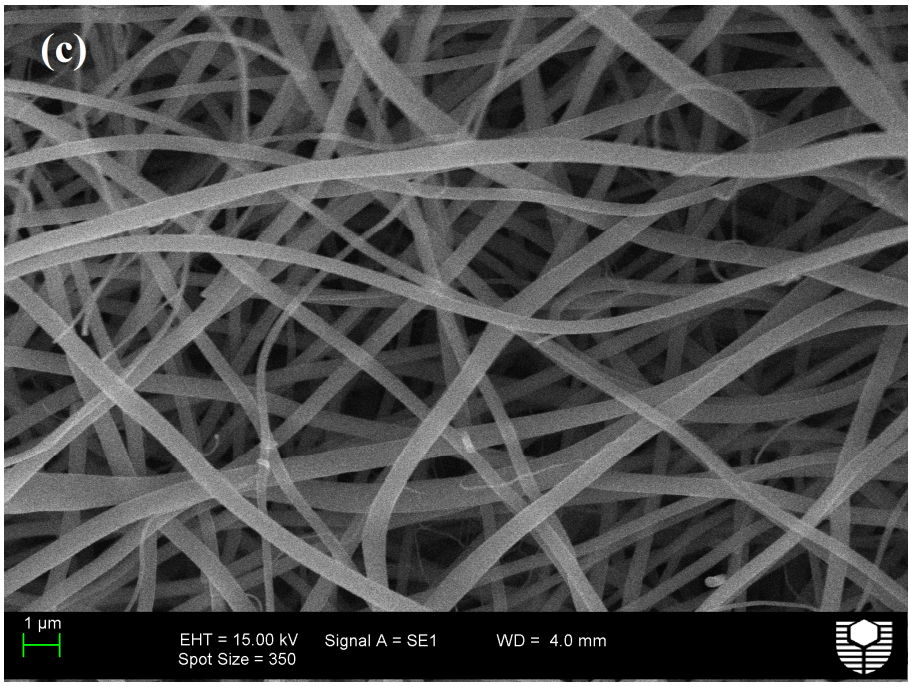
(c)
1 µm
EHT = 15.00 kV
Spot Size = 350
Signal A = SE1
WD = 4.0 mm

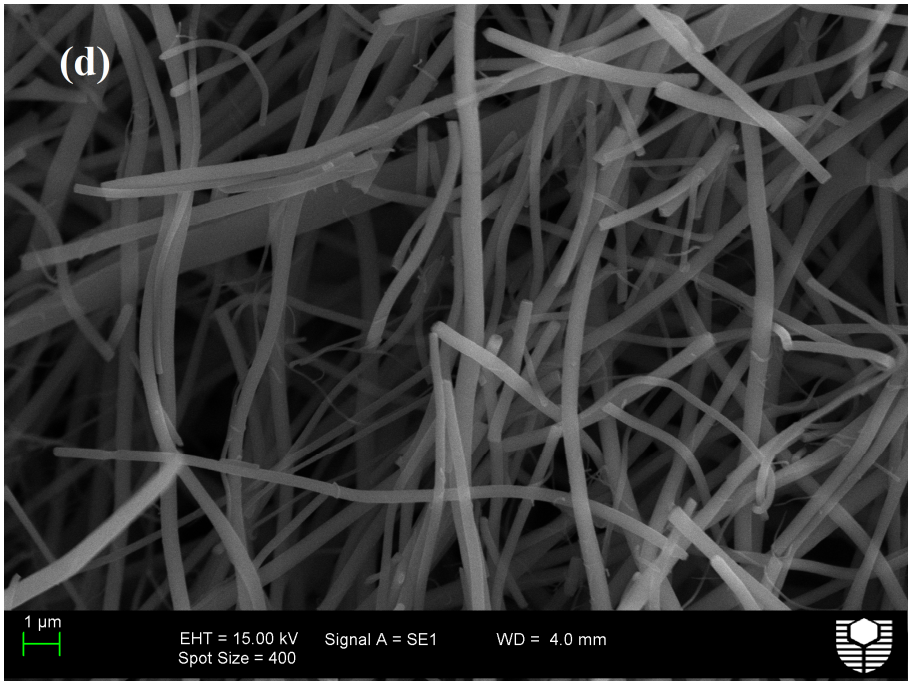
(d)
1 µm
EHT = 15.00 kV
Spot Size = 400
Signal A = SE1
WD = 4.0 mm

Figure 1

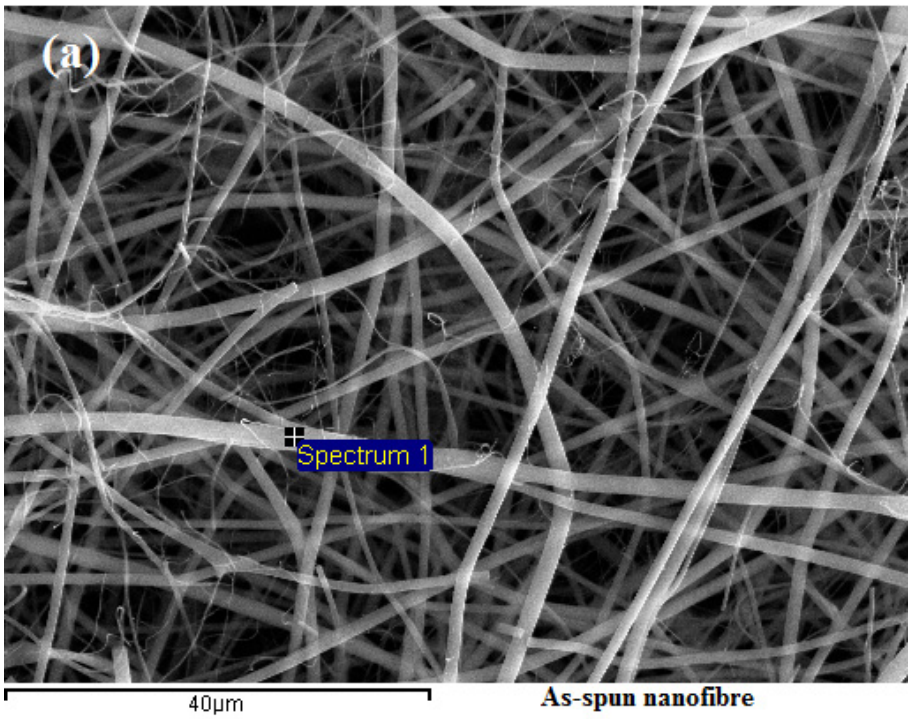

As-spun nanofibre

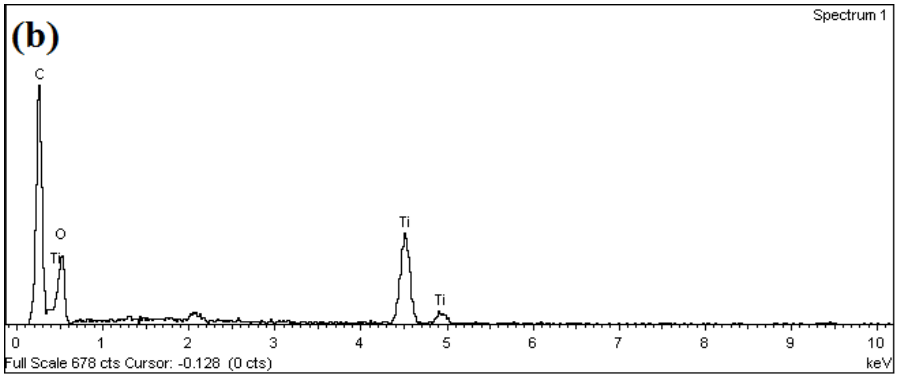

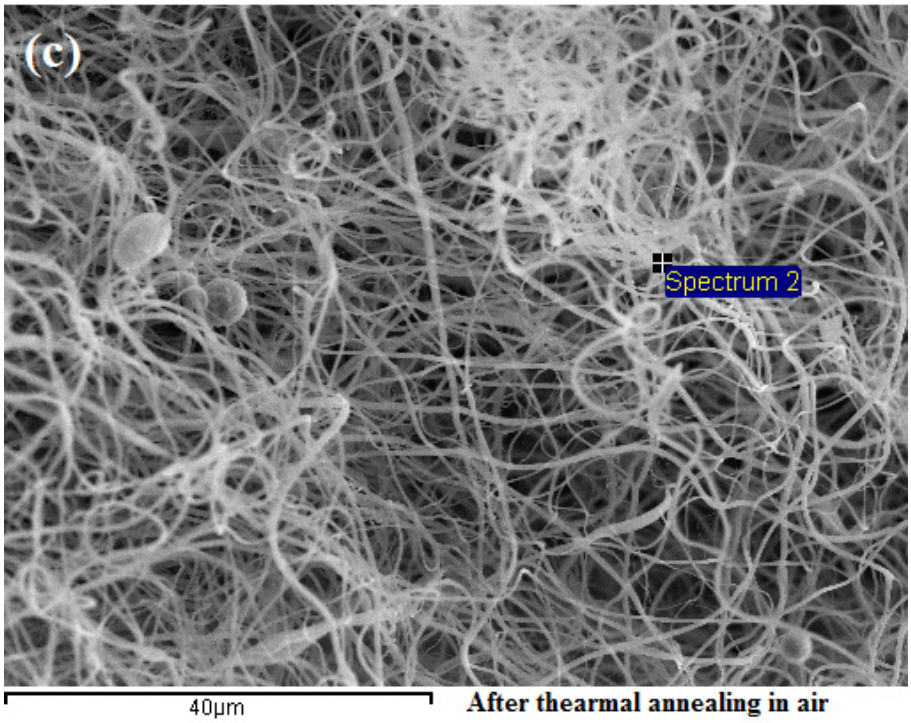
(c)
Spectrum 2
40μm
After thearmal annealing in air

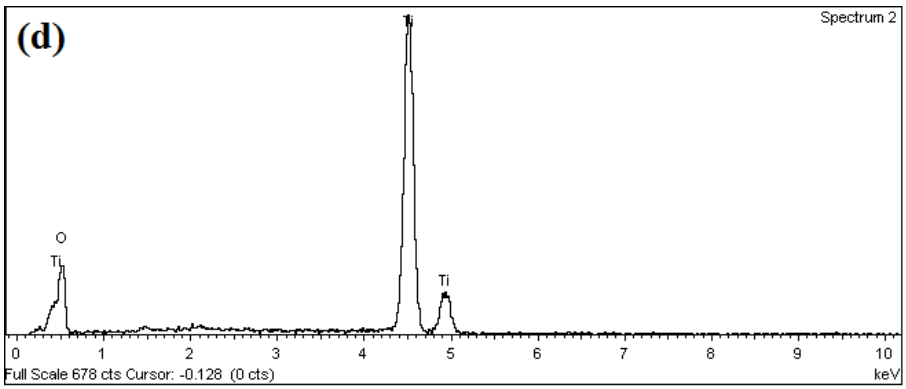
(d)
Spectrum 2
O
Ti
Ti
Ti
0
1
2
3
4
5
6
7
8
9
10
Full Scale 678 cts Cursor: -0.128 (0 cts)
keV

Figure 2

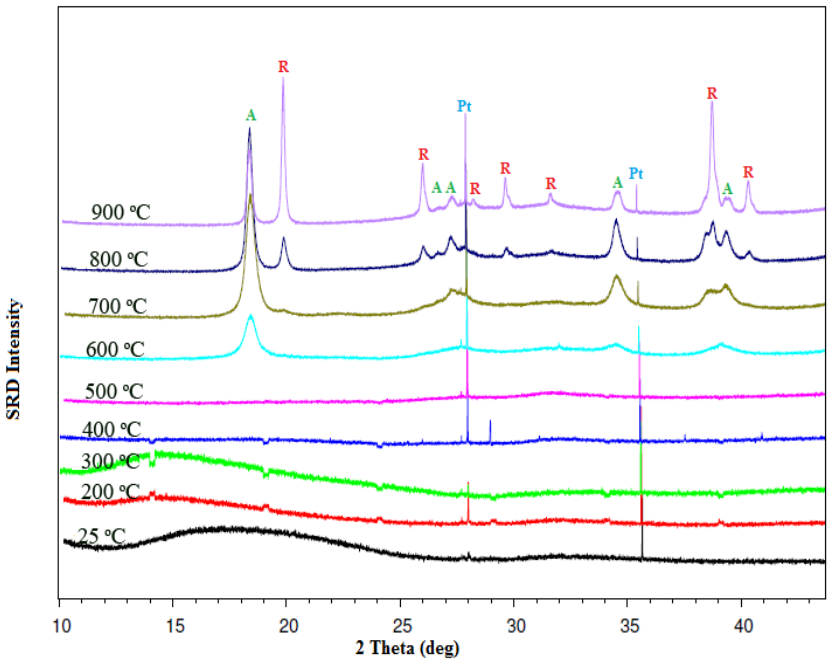

Figure 3.a

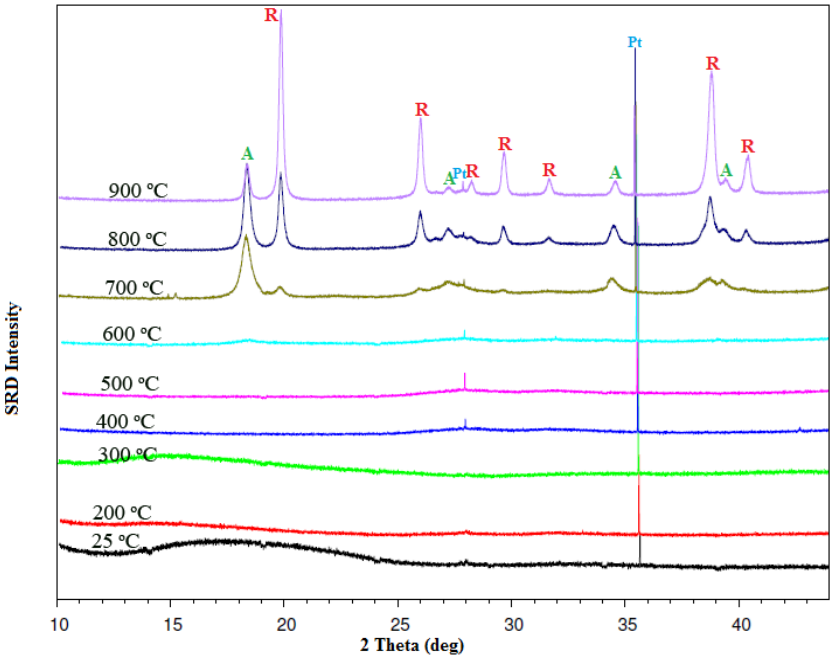

Figure 3.b

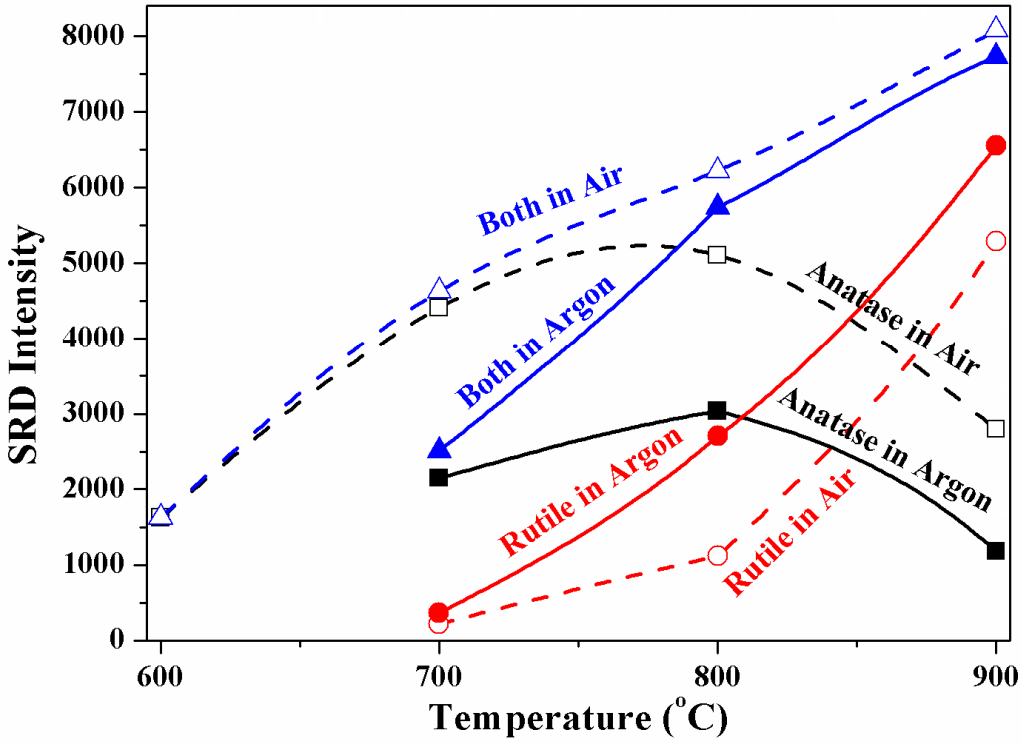
SRD Intensity
8000
7000
6000
5000
4000
3000
2000
1000
0
600
700
800
900
Temperature (°C)
Both in Air
Both in Argon
Anatase in Air
Anatase in Argon
Rutile in Argon
Rutile in Air

Figure 4

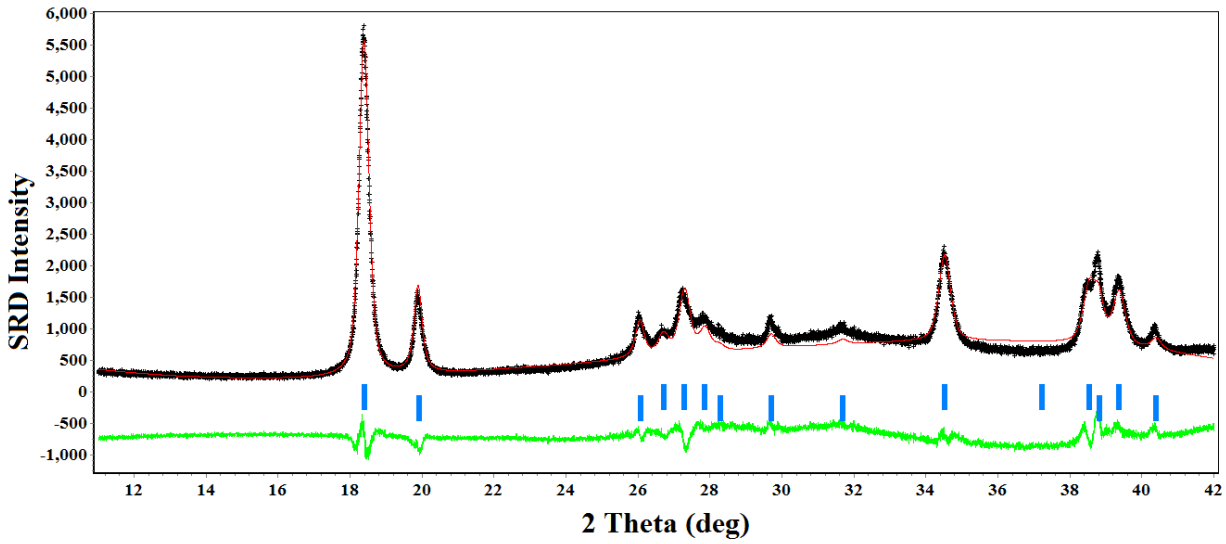

Figure 5.a

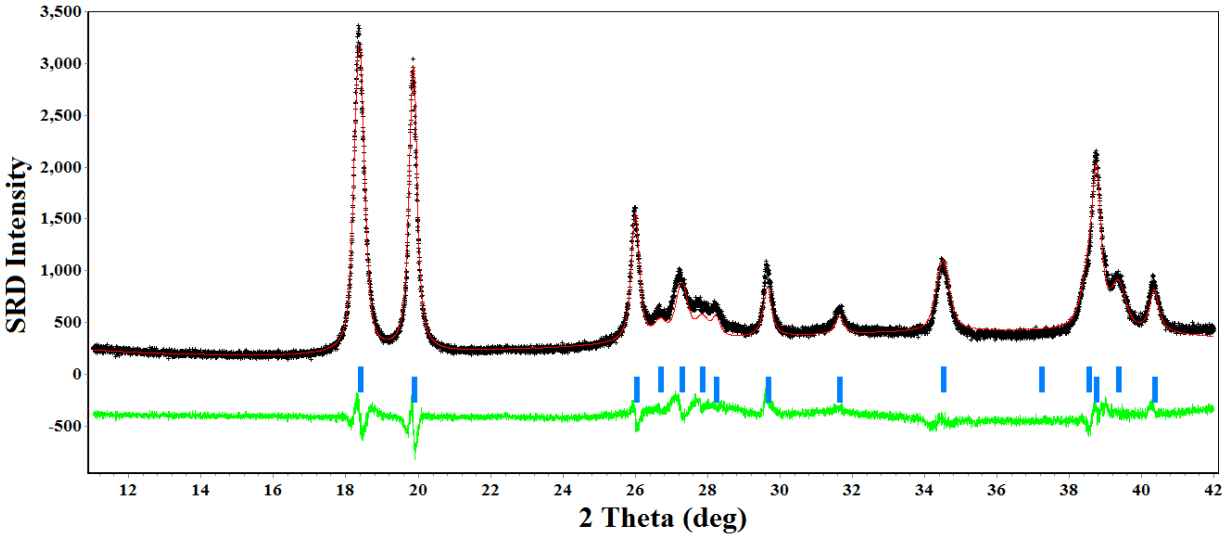

Figure 5.b

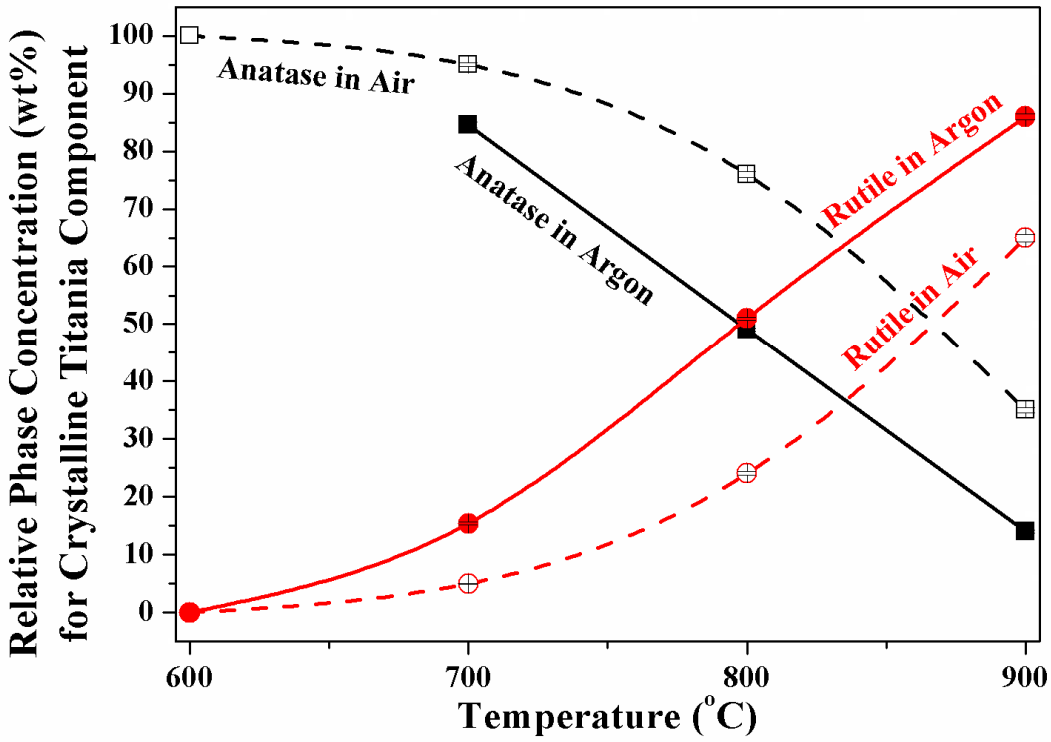
Relative Phase Concentration (wt%)
for Crystalline Titania Component
100
90
80
70
60
50
40
30
20
10
0
600
700
800
900
Temperature (°C)
Anatase in Air
Anatase in Argon
Rutile in Argon
Rutile in Air

Figure 6

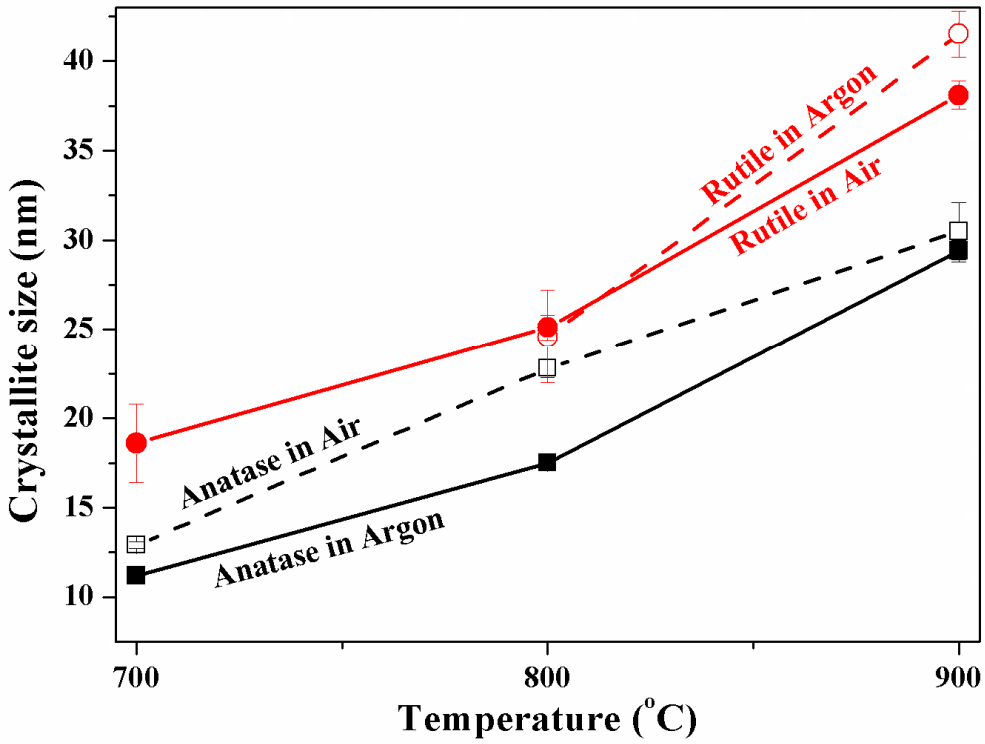
Crystallite size (nm)
40
35
30
25
20
15
10
700
800
900
Temperature (°C)
Rutile in Argon
Rutile in Air
Anatase in Air
Anatase in Argon

Figure 7

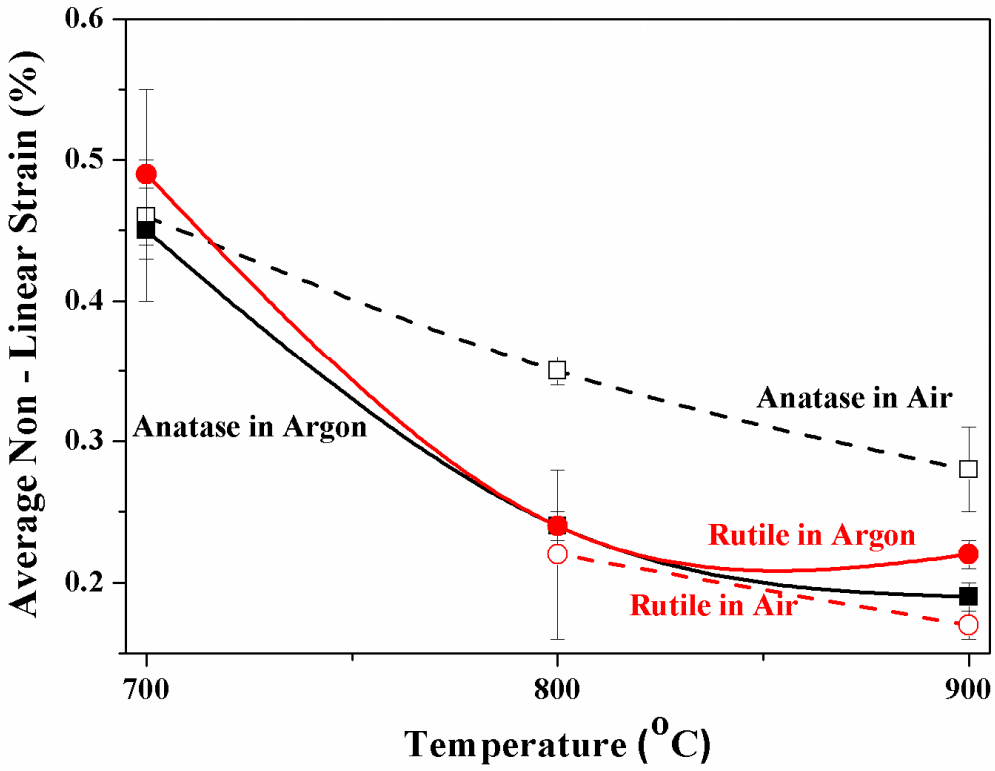
0.6
0.5
0.4
0.3
0.2
Average Non - Linear Strain (%)
Anatase in Air
Anatase in Argon
Rutile in Argon
Rutile in Air
700
800
900
Temperature (°C)

Figure 8

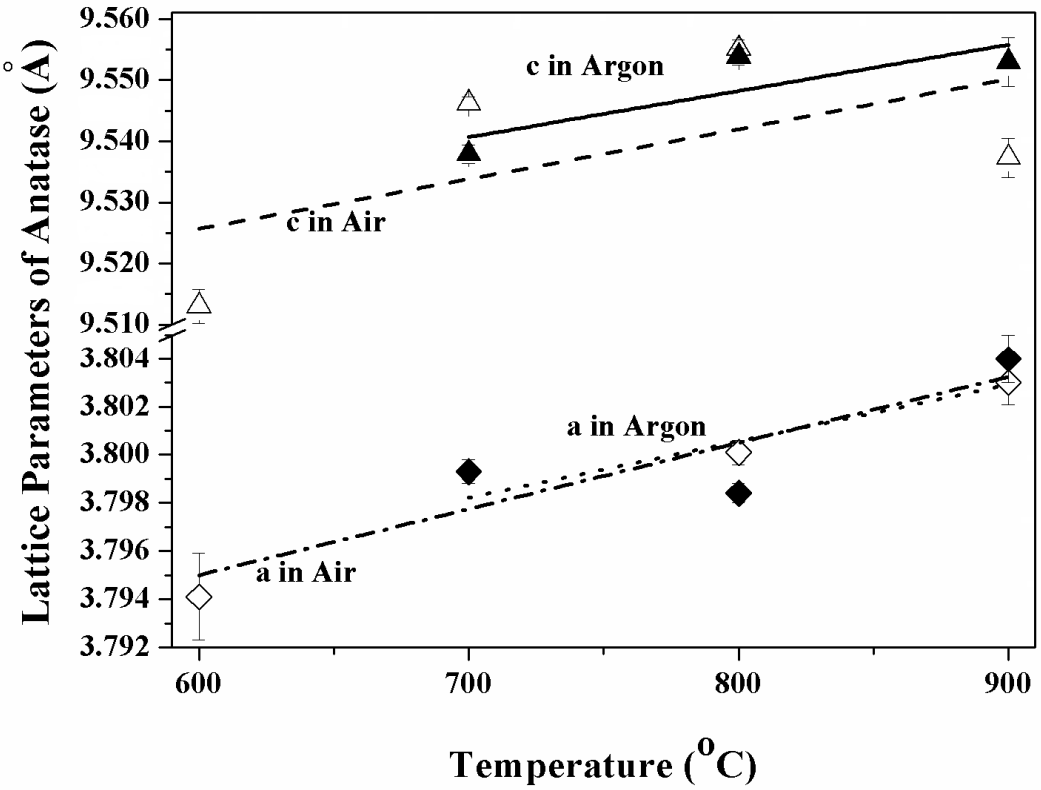
Lattice Parameters of Anatase (Å)
9.560
9.550
9.540
9.530
9.520
9.510
3.804
3.802
3.800
3.798
3.796
3.794
3.792
c in Argon
c in Air
a in Argon
a in Air
600
700
800
900
Temperature (°C)

Figure 9.a

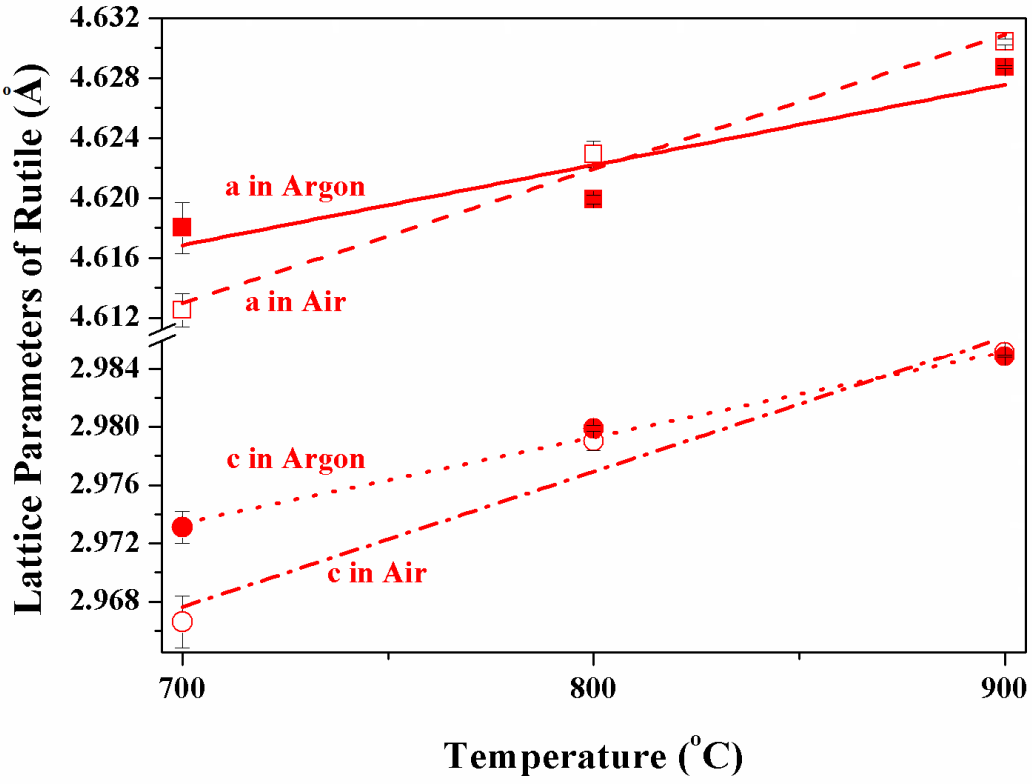
Lattice Parameters of Rutile (Å)
4.632
4.628
4.624
4.620
4.616
4.612
2.984
2.980
2.976
2.972
2.968
a in Argon
a in Air
c in Argon
c in Air
700
800
900
Temperature (°C)

Figure 9.b

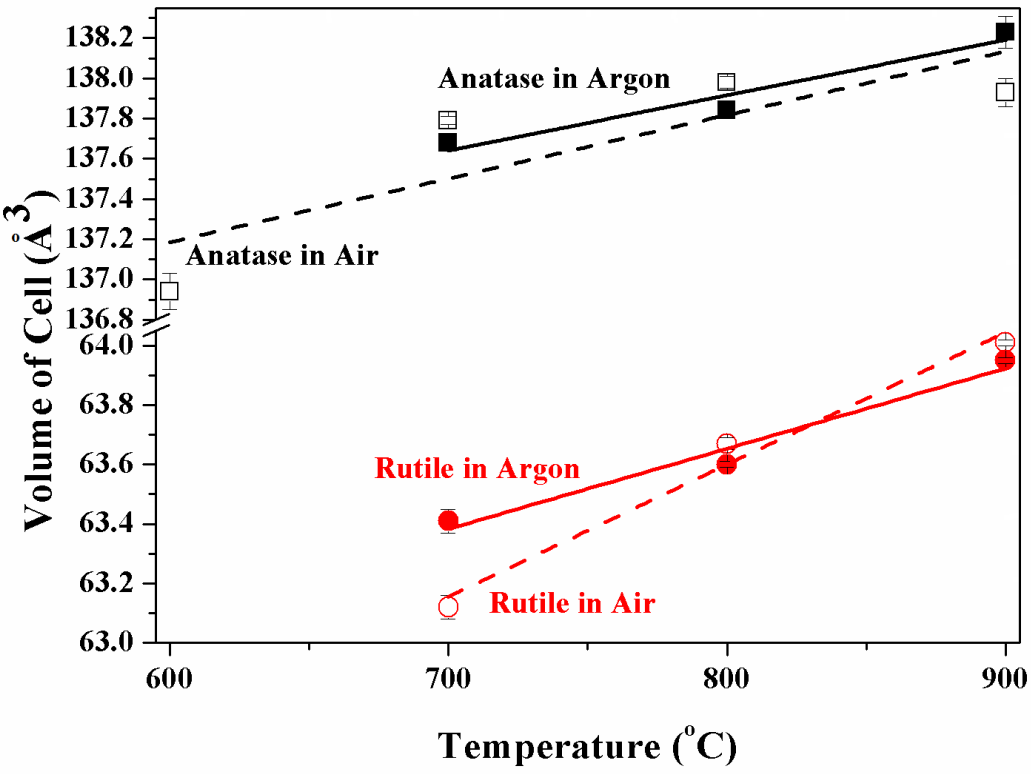
Anatase in Argon
Anatase in Air
Rutile in Argon
Rutile in Air
Volume of Cell (Å^3)
Temperature (^{o}C)
138.2
138.0
137.8
137.6
137.4
137.2
137.0
136.8
64.0
63.8
63.6
63.4
63.2
63.0
600
700
800
900

Figure 10